Article:
Lo Conte, R, Martinez, E, Hrabec, A et al. (11 more authors) (2015) Role of B diffusion in the interfacial Dzyaloshinskii-Moriya interaction in Ta / Co_{20} $Fe_{60}B_{20}$/MgO nanowires. Physical Review B, 91 (1). 014433. ISSN 1098-0121

https://doi.org/10.1103/PhysRevB.91.014433

Role of B diffusion in the interfacial Dzyaloshinskii-Moriya interaction in Ta\$Co_{20}Fe_{60}B_{20}$\MgO nanowires

R. Lo Conte,[1,2] E. Martinez,[3] A. Hrabec,[4] A. Lamperti,[5] T. Schulz,[1] L. Nasi,[6] L. Lazzarini,[6] R. Mantovan,[5] F. Maccherozzi,[7] S. S. Dhesi,[7] B. Ocker,[8] C. H. Marrows,[4] T. A. Moore,[4] and M. Kläui[1,2]

[1]*Johannes Gutenberg Universität-Mainz, Institut für Physik, Staudinger Weg 7, 55128 Mainz, Germany*
[2]*Graduate School of Excellence Materials Science in Mainz (MAINZ), Staudinger Weg 9, 55128 Mainz, Germany*
[3]*Dpto. Fisica Aplicada, Universidad de Salamanca, plaza de los Caidos s/n E-38008, Salamanca, Spain*
[4]*School of Physics and Astronomy, University of Leeds, Leeds LS2 9JT, U.K.*
[5]*Laboratorio MDM, IMM-CNR, via C. Olivetti 2, 20864 Agrate Brianza (MB), Italy*
[6]*IMEM-CNR, Parco Area delle Scienze 37/A, 43124 Parma (PR), Italy*
[7]*Diamond Light Source, Chilton, Didcot, Oxfordshire, OX11 0DE, U.K.*
[8]*Singulus Technologies AG, 63796 Kahl am Main, Germany*

We report on current-induced domain wall motion (CIDWM) in Ta\$Co_{20}Fe_{60}B_{20}$\MgO nanowires. Domain walls are observed to move *against* the electron flow when no magnetic field is applied, while a field along the nanowires strongly affects the domain wall motion velocity. A symmetric effect is observed for up-down and down-up domain walls. This indicates the presence of right-handed domain walls, due to a Dzyaloshinskii-Moriya interaction (DMI) with a DMI coefficient D=+0.06 mJ/m^2. The positive DMI coefficient is interpreted to be a consequence of B diffusion into the Ta buffer layer during annealing, which was observed by chemical depth profiling measurements. The experimental results are compared to 1D-model simulations including the effects of pinning. This modelling allows us to reproduce the experimental outcomes and reliably extract a spin-Hall angle θ_{SH}=-0.11 for Ta in the nanowires, showing the importance of an analysis that goes beyond the model for perfect nanowires.

I. INTRODUCTION

The demand for data storage devices able to store information at increasingly high densities has led to an enormous effort investigating materials systems useful for such a purpose. In information and communication technology magnetic materials are used extensively [1]. Nowadays, scientific interest is moving from single magnetic materials-based systems [2] to more complicated hetero-structures [3]. The latter are materials systems characterized by perpendicular magnetic anisotropy (PMA) and structural inversion asymmetry. The PMA results in domain wall (DW) widths of a few nm [4], which offer the opportunity of a high data-storage density. Examples of such materials stacks are Pt\Co\$AlO_x$ [5-8], Pt\$[Co\Ni]_x$\Co\TaN [3], Ta\CoFe\MgO [9] and Ta\CoFeB\MgO [10-13], which have a magnetization pointing out of the plane and no inversion symmetry in the vertical direction. Very effective current-induced domain wall motion (CIDWM) [3,5,7] and magnetization switching [14-17] have been observed in nanostructures made of such materials. After the first experimental observations, the Rashba effect [6,18] and the spin-Hall effect (SHE) [14,19,20] were considered to be the leading causes for the magnetization dynamics in such systems. More recent results support the interpretation that the SHE is likely to be the main cause [3,9]. According to the spin-orbit torque (SOT)-model, the symmetry of the resulting torque is defined by the SHE generated in the heavy metal underlayer and the Dzyaloshinskii-Moriya interaction (DMI) that is governed by the interface between the heavy metal and the magnetic layer [3,9,21,22]. In this scenario the DMI fixes the chirality of the domain walls [22].

Much attention has been dedicated to systems such as Ta\CoFeB\MgO, due to the fact that this materials stack is already used for the fabrication of spintronic devices [23] whose functionality is based on the spin-transfer torque (STT) [24]. With the discovery of the SOTs, the next challenge is to understand what exactly governs the torques and the DMI strength and sign. First steps forward in the understanding of the symmetry of the torque have been taken, measuring the angular dependence of the generated effective fields [12,13]. However, in those experiments only the mono-domain state of a magnetic nanostructure was probed. Instead, for the dynamics of domain walls the DMI starts to play an important role, so that in order to learn more about such an

interaction it is necessary to carry out DWM experiments. Recently, the effects of different underlayers including Ta and TaN were studied and found to impact the DWM [25] but at the moment it is not clear to what extent the underlayer or the interface play a role and therefore further studies including structural characterization are needed.

Here we report a comprehensive study of CIDWM in out-of-plane magnetized Ta\$Co_{20}Fe_{60}B_{20}$\MgO nanowires. The DW velocity is measured in the presence of a variable external magnetic field applied along the wire axis. A strong effect of this longitudinal field on the DW motion is observed, allowing us to measure the DMI strength D for the hetero-structure under investigation. Diffusion and consequent segregation of boron at the Ta\CoFeB interface are found by chemical depth profiling measurements, suggesting that they play an important role in governing the interfacial DMI in our system. Comparing experiments to 1D-model simulations, we are able to understand the role of the pinning in the DW dynamics and extract the value of the spin-Hall angle of Ta in the nanowires with high confidence.

II. SAMPLES AND EXPERIMENTAL SET-UP

Our sample consists of Ta(5nm)\$Co_{20}Fe_{60}B_{20}$(1nm)\MgO(2nm)\Ta(5nm) deposited on a thermally oxidized Si-wafer. The entire materials stack is deposited by sputtering (using a Singulus TIMARIS/ROTARIS tool), and then annealed at 300 ˚C for 2 hours in vacuum so that a large PMA is obtained. From growth studies it is known that the Ta bottom layer grows for our deposition conditions and thicknesses largely in the β-phase, and for our sample this is confirmed by its high measured resistivity (180 μΩ·cm). For a measured in-plane magnetization saturation field $\mu_0 H_{sat}$=400 mT and a saturation magnetization $M_s=1.1\times10^6$ A/m (measured by SQUID), we obtain an effective anisotropy $K_{eff}=\mu_0 H_{sat} M_s/2=2.2\times10^5$ J/m^3. By electron-beam lithography and argon-ion milling the sample is then patterned into an array of 20 nanowires in a parallel geometry (see Fig. 1(a)). The dimensions of each wire are 1 μm x 8 μm. At the ends of the wires there are magnetic pads, directly connected to two gold contact pads made in a second patterning step by a lift-off technique. One of the two gold pads consists of an Oersted-line, used for the nucleation of reversed magnetic domains in pre-saturated wires, by the injection of 20 ns-long current pulses.

As shown in Fig. 1(a), a pulse generator is used for injecting current through either the Oersted-line or the magnetic wires. An oscilloscope is used for measuring the pulse waveform, across its 50 Ω-internal resistance (R_o). The total current flowing through the system is obtained by the measured voltage V_o across R_o. Taking into account the oxidation of the top 2 nm of the Ta capping layer (see Fig. 5(a)), we estimate a current density of 1.1×10^{11} A/m^2 flowing through the nanowires when 1 V drops across R_0 (corresponding to a total current of 20 mA). The conventional current density j_a is assumed to be positive when it flows in the +x-direction (see Fig. 1), so that the electron current density $j_e<0$ is in the +x-direction. The magnetization configuration of the wires is imaged by polar Kerr microscopy in differential mode. A magnetic coil is used for the generation of an external in-plane magnetic field. The experiments are carried out at T=300 K. We first saturate the magnetic wires in the up (+z)- or down (-z)-magnetization state, then we nucleate reversed domains either by the Oersted-line or injecting a current pulse through the wires. By the injection of an Oersted-pulse we generate only one type of domain wall (DW), either up-down (↑↓)- or down-up (↓↑)-DW. On the other hand, we generate both types of DWs by injecting current through the nanostructures, due to current-induced magnetization switching [17]. Fig. 1(b) and 1(c) show controlled domain nucleation by current through the Oersted-line and DW displacement due to the injection of a burst of negative current pulses ($j_a<0$) in the wires, respectively.

III. CURRENT-INDUCED DOMAIN WALL MOTION

Fig. 2 reports the average velocity of the DW as a function of the current density flowing through the magnetic wires. For each current density the measurement is repeated three times, yielding a total of 30 DW displacements (10 nanowires are imaged at the same time). This allows us to obtain sufficient statistics for the DW motion details. Bursts of several (n) current pulses with a time duration Δt=10, 15, 20 and 25 ns are used for the CIDWM (see Fig. 2(a)). The time between two consecutive pulses is 100 μs and the number of pulses in a burst ranges from n=20 to n=400. The velocity of the DW is calculated as the ratio between the displacement of the domain wall due to the injected pulse burst and the total pulsing time $T=n*\Delta t$. With the measurements for the different pulse lengths it is possible to rule out the effect of the rise and fall-time (5 ns each in our

experimental set-up) on the measured DW velocity. Indeed, as shown in Fig. 2(a), higher velocities are measured for longer pulse lengths at a fixed current density. This is because the rise/fall time takes up a smaller proportion of the overall pulse length Δt, enabling the torque on the DW to be larger for a greater fraction of the pulse time. This has to be taken into account when comparing results for different Δt. In Fig. 2(b) the resulting average DW velocity free of the influence of the rise- and fall-time is shown. One of the key pieces of information in Fig. 2 is the direction of the DW velocity: the DWs move against the electron flow. This is a clear indication of the fact that in our system the DWs are not moved by conventional STT [24], which would move them in the electron flow direction. Instead, the observed DWM is in agreement with the SOT-model [3,9,22]. A similar interpretation was given for Pt\CoFe\MgO and Ta\CoFe\MgO systems [9], where the authors claimed that the DWM is due to the SHE-effective field $\boldsymbol{H}_{SHE} = \hbar\theta_{SH}|j_e|/(2\mu_0|e|M_sL_z)(\hat{\boldsymbol{m}} \times (\hat{\boldsymbol{z}} \times \hat{\boldsymbol{j_e}}))$, where θ_{SH} is the spin-Hall angle (SHA), j_e is the electron-current density, M_s is the saturation magnetization of the ferromagnetic material and L_z is the thickness of the ferromagnetic layer. However, in our experiments the DWM is in the opposite direction to that in Ta\CoFe\MgO [9]. The main difference between the material system in [9] and the stack investigated here is the presence of boron (B) in the ferromagnetic layer, which lends itself to an interpretation of the present observations based on the effect of the B. Accordingly, the reasons for the observed DWM being in the opposite direction to that observed in [9] will be discussed in detail below.

IV. CHIRAL DOMAIN WALLS

Next we report the effect of magnetic fields on CIDWM. More precisely, the DW velocity is measured as a function of an applied magnetic field along the wire axis (x-direction) for fixed current densities (see Fig. 3). First of all, both types of DW (↑↓ and ↓↑) are nucleated in the pre-saturated nanostructures by current-induced magnetization switching (see Fig. 3(a)). Typical nucleation pulses used in the experiment have a current density j_a~10^{12} A/m^2 and a duration Δt=20 ns. Once the DWs are generated, they are displaced by injecting a burst (n=1-20) of 20 ns-long current pulses with lower current densities (2.8-3.6x10^{11} A/m^2), as shown in Fig. 3(b). In order to calculate the DW velocity, the full width at half maximum of the current pulse is used as the time

duration of a single pulse. For each current density-field amplitude combination the measurement is repeated five times. The DW velocity as a function of the longitudinal field $\mu_0 \mathbf{H_x}$ is shown in Fig. 3(c) and 3(d) (symbols), respectively for the ↓↑- and ↑↓-DWs. The graphs show that the DW velocity is strongly influenced by the presence of the longitudinal field. While at zero field the velocity of both types of DWs is the same, in the presence of the field the two DWs move at different velocities. We observe a symmetric behavior of the DW velocity as a function of $\mu_0 \mathbf{H_x}$ for the two types of DW, as shown in Fig. 3(e) (solid symbols for the ↑↓-domain wall, empty symbols for the ↓↑-domain wall). Similar observations have been reported for magnetic structures made of several different materials stacks [3,9,25].

To understand these observations, including the motion of DWs against the electron flow reported above, we need to consider possible mechanisms. According to the standard STT-model [24] the DWs are expected to move always with the electron flow, unless the magnetic layer where the DWs are moved exhibits a negative spin polarization or a negative non-adiabaticity constant. However, to our knowledge neither of these have been reported experimentally so far. Secondly, one would not expect such a strong effect of a longitudinal magnetic field on the motion of the DWs in the case that the standard STT is the driving force in the DW dynamics. Furthermore STT cannot explain why for longitudinal fields the DW can stop moving of even change its motion direction. This means, we need to look for a different interpretation for our experimental data.

In the SOT-model, the magnetic domain wall can both move with or against the electron flow depending on the SOTs and the domain wall spin structure, in particular its chirality. The driving force for the DW dynamics is the pure spin-current induced by the SHE generated in the heavy metal during the pulse injection. Furthermore, the DMI at the interface between the heavy metal and the ferromagnetic layer is responsible for the initial magnetic configuration and in particular the chirality of the DW [22,26], governing the direction of motion. As a consequence, the direction of the DWM depends on both the sign of the SHA and the sign of the DMI, where the latter fixes the chirality (left- or right-handed) of the Néel-component of the DW. The SHA of Ta is known to have a negative sign, as reported in the literature by other groups for different materials stacks [9,27] as

well as determined by us in a previous work for the very same material system used here [17]. So far only few reports have studied the DMI in [heavy metal underlayer]\CoFeB\MgO systems [25] and a strong dependence on the underlayer material and thickness was found. So here we analyze our data within the SOT-model framework to extract the key parameters such as the SHE and the DMI for the used material stack.

When an interfacial DMI is present, it acts on the magnetic texture as a longitudinal effective field localized at the domain wall position [22]. This field is known as the DMI effective field and is defined as $\mu_o H_{DMI}=D/(M_S \Delta)$ [22,28], where D is the DMI coefficient, and Δ is the DW width. Accordingly, the applied longitudinal field at which the SOT is minimized, resulting in a stationary DW, is the so-called stopping field, that is of the same amplitude as and of opposite sign to H_{DMI}, (assuming that there is no significant STT). However, Fig. 3(c), (d) and (e) show that there is a range of in-plane longitudinal fields $\mu_o \mathbf{H}_x$ where the DW remains stationary (with zero or very small DW velocity compared to the velocities measured for larger longitudinal fields). This zero motion field range is not reproduced by the standard SOT-DWM model. As shown later, in order to properly analyze the experimental data a more accurate model is needed, where this "pinning" effect is taken into account.

Since the reversal of the direction of the DW motion occurs in the low-velocity field range, a more detailed analysis of this behavior follows. The DMI-field is extracted by linearly fitting the experimental data in Fig. 3(e), for both types of DW and for both positive and negative current. Considering only the high velocity experimental data, the crossing of the two best fitting lines for the ↑↓-DW data occurs at a longitudinal field value $\mu_o H_x^{\uparrow\downarrow}$=-8.5±1.8 mT, while for the ↓↑-DW the crossing occurs at $\mu_o H_x^{\downarrow\uparrow}$=+7.0±1.5 mT. Assuming the amplitude of the DMI field to be the average of the two fields (in absolute values) we obtain $|\mu_o H_{DMI}|$=7.8±1.2 mT. All the errors correspond to one standard deviation. Since the DW width is Δ=7 nm ($\Delta=(A/K_{eff})^{1/2}$, where we use $A=10^{-11}$ J/m [28]), $\mu_o H_x^{\uparrow\downarrow}<0$ and $\mu_o H_x^{\downarrow\uparrow}>0$, and knowing that Ta-$\theta_{SH}$ has a negative sign [9,17,27] we obtain a DMI constant D=+0.06±0.01 mJ/m^2. Such a value is close to the one measured for the Ta\CoFe interface [28], but of opposite sign, indicating the presence of right-handed DWs in our nanowires,

while left-handed DWs were reported for Ta\CoFe\MgO nanowires [28]. This provides a reason for the DWM we observe being opposite to that in Ta\CoFe\MgO [9].

V. BORON DIFFUSION AND SEGREGATION

In the search of an explanation for the positive DMI coefficient observed here, it is important to note that the material stack was annealed at 300 °C for 2 h in vacuum. This was done in order to obtain a strong PMA. As the DMI and the SOTs depend strongly on the interface, we use high resolution transmission electron microscopy (HRTEM) imaging and secondary ion mass spectrometry (SIMS) as tools to investigate the structural properties of the materials stack. The TEM cross-section image in Fig. 4(a) confirms the nominal thickness of each layer composing the stack, and provides evidence for the presence of a top Ta-oxide layer due to the natural Ta oxidation in air. The interfaces are smooth and well defined; in particular the MgO\Ta interface retains sub-nanometer topographical roughness after the crystallization of the MgO and CoFeB layers upon annealing, in agreement with other reported results [29]. The TEM image also shows the crystallization of MgO and CoFeB. Furthermore, time-of-flight SIMS depth profiling in Fig. 4(b) on exactly the same materials stack clearly shows that B diffuses out of the CoFeB layer into the MgO and into the Ta-layer during the annealing process. Considering, in detail, the B profile in Fig. 4(b) for the as-deposited (empty symbols) and the annealed (full symbols) stack, it is observed that the profile related to the annealed stack shows: *(i)* a reduced B intensity in the CoFeB layer; *(ii)* an increased B intensity in the region corresponding to the underneath Ta layer; *(iii)* a different modulated intensity close to the MgO\CoFeB interface. This is direct evidence for B diffusion from CoFeB to the adjacent layers, thus affecting in particular Ta\CoFeB interface where B segregation is expected [30]. Since the DMI is expected to be a function of the structure and in particular the atomic arrangement at the interface [21,25,26], the B accumulation at the Ta\CoFeB interface can play a major role in the generation of the positive DMI, in particular given that this presence of B is the key difference compared to CoFe-based material stacks which exhibit negative DMI. The idea that a strong accumulation of B in the bottom Ta-layer could be responsible for the character of the DMI is supported by previous works where it was reported that an N-doped Ta bottom layer can

change the DMI sign compared to the case of pure Ta\CoFeB system [25]. Using the theory put forward in [25], one explains similarly to the case of N-doping in Ta that the large accumulation of B in Ta (as observed in our material system) and the larger electronegativity of B with respect to Ta leads to a change in the electronic configuration at the Ta\CoFeB interface due to 5d-2p hybridization of the electron wave function. Thus our observation of the sign change is an important test of this model using an independently fabricated and measured set of samples and our results corroborate the theoretical explanation. The observation of a positive DMI in our system is furthermore supported by the recent report of right-handed DWs in a Ta\CoFeB\TaO_x system [31]. Finally, our observation of current-induced DW motion with the electron flow in nanowires made of Pt\CoFeB\MgO (for details, see supplemental material [32]) suggests again that the B presence in the system influences the character of the interfacial DMI. However, for a more quantitative understanding of the effect of B, a systematic study is needed, which is beyond the scope of this paper.

VI. DMI AND SHE EXTRACTION BY 1D-MODELLING

To quantify the DMI and the SHE we analyze the DW velocities in Ta\$Co_{20}Fe_{60}B_{20}$\MgO nanowires shown in Fig. 3(c)-(e) in more detail. As stated above, there is a range of longitudinal magnetic fields for which the DW stops moving or it moves with a very low average velocity. However, when the longitudinal field reaches a certain value the domain wall velocity increases suddenly. Here an interpretation of such observations is offered, based on a 1D-model including DW pinning effects.

In the framework of the 1D-model (1DM), the DW dynamics is described in terms of the DW position X and the DW angle Φ by the following equations [9,33]

$$(1+\alpha^2)\frac{1}{\Delta}\frac{dX}{dt} = Q\Omega_A + \alpha\Omega_B \quad (1)$$

$$(1+\alpha^2)\frac{d\Phi}{dt} = -\alpha\Omega_A + Q\Omega_B \quad (2)$$

with

$$\Omega_A = -\frac{\gamma_0}{2}H_K \sin(2\Phi) + \gamma_0\frac{\pi}{2}H_x \sin(\Phi) - Q\,\gamma_0\frac{\pi}{2}H_{DMI}\sin(\Phi)$$

$$\Omega_B = Q\gamma_0 \frac{\pi}{2} H + \mathrm{Q}\,\gamma_0 \frac{\pi}{2} H_{SHE} \cos(\Phi),$$

where $\Delta=(A/K_{eff})^{1/2}$=7 nm is the DW width with $K_{eff}=K_u-\mu_\circ M_s^2/2$, where K_u=9.8x10^5 J/m^3 is the PMA anisotropy constant, A=10^{-11} J/m is the exchange constant and M_s=1.1x10^6 A/m the saturation magnetization. These inputs correspond to the experimentally deduced value for K_{eff}=2.2x10^5 J/m^3. $H_K=N_xM_s$ is the shape anisotropy field with $N_x=L_zLog(2)/(\pi\Delta)$ being the magnetostatic factor [34]. α=0.013 is the Gilbert damping [35]. L_z=1 nm is the thickness of the ferromagnetic layer and L_y=1000 nm its width. The factor Q=+1 and Q=-1 for the ↑↓ and ↓↑ configurations respectively. In the framework of the 1DM, the DMI generates an effective field along the *x*-axis with amplitude given by [22] $H_{DMI} = \frac{D}{\mu_0 M_s \Delta}$, where D is the DMI parameter. H_{SHE} is the effective spin-Hall field given by [36] $H_{SHE} = \frac{\hbar\theta_{SH} j_a}{2e\mu_0 M_s L_z}$, where θ_{SH} is the spin Hall angle, e is the electron charge and j_a is the current density ($\boldsymbol{j_a}=j_a\boldsymbol{u_x}$ and $\boldsymbol{j_e}=j_e\boldsymbol{u_x}$, with j_a>0 along the +x-direction and j_e=-j_a). H_x is the applied longitudinal field along the *x*-axis, and $H=H_{pin}+H_{th}$ includes the pinning field $H_{pin}(X)$ and the thermal field H_{th}. The spatially-dependent pinning field accounts for local imperfections (such as edge or surface roughness or defects), and can be derived from an effective spatially-dependent pinning potential $V_{pin}(X)$, thus [37]

$$H_{pin}(X) = -\frac{1}{2\mu_0 M_s L_y L_z} \frac{\partial V_{pin}}{\partial X}.$$

A periodic potential was assumed to describe the experimental results

$$V_{pin}(X) = V_0 \sin(\frac{\pi X}{p}),$$

where V_0 is the energy barrier of the pinning potential and p is its spatial period. Finally, the thermal field $H_{th}(t)$ describes the effect of thermal fluctuations, and it is assumed to be a random Gaussian-distributed stochastic process with zero mean value ($< H_{th}(t) >= 0$), uncorrelated in time ($< H_{th}(t)H_{th}(t') >= \frac{2\alpha K_B T}{\gamma_0\mu_0 M_s \Delta L_y L_z}\delta(t-t')$), where K_B is the Boltzmann constant and T the temperature [34]. The 1DM results were computed at T=300 K. Eqs. (1) and (2) were numerically solved by means of a 4th-order Runge-Kutta algorithm with a time step of 1ps over a temporal window of 100 ns.

The experimental results for the CIDWM are accurately reproduced by the 1DM predictions if we assume a DMI constant D=+0.06 mJ/m^2 and a SHA θ_{SH}=-0.11, a pinning potential V_0=7x10^{-20} J and p=21 nm as can be seen in Fig. 3(c), (d) and (e). The pinning potential parameters were selected to reproduce the experimentally observed propagation field (H_p≈5 Oe) in the absence of a current. It is interesting to note that the deduced positive DMI coefficient results in right-handed chiral Néel walls in the absence of a current and field (j_a=H_x=0), as already said in IV. Therefore, the internal magnetization ($\mathbf{m}_{DW}$) of an ↑↓- (↓↑-) domain wall points along the positive (negative) x-axis ($\mathbf{m}_{DW}$≈±$\mathbf{u}_x$). The extracted SHA value is in agreement with other values reported in literature [27,28].

Let us focus firstly on the ↑↓-domain wall case. Consistent with the negative value of the SHA for Ta, it is clear from Fig. 2 that the DW moves against the electron flow in the absence of longitudinal field. As already discussed, the effective field associated with the SHE is given by

$$\mathbf{H}_{\mathrm{SHE}} = \frac{\hbar\theta_{\mathrm{SH}}}{2\mathrm{e}\mu_0 \mathrm{M_s L_z}}\left[\mathbf{m}_{\mathrm{DW}} \times (\mathbf{u}_{\mathrm{z}} \times \mathbf{j}_{\mathrm{a}})\right] = \frac{\hbar\theta_{\mathrm{SH}} \mathrm{j_a}}{2\mathrm{e}\mu_0 \mathrm{M_s L_z}} \mathrm{m}_{\mathrm{DW,x}} \mathbf{u}_{\mathrm{z}} = \mathrm{H}_{\mathrm{SHE}} \mathrm{m}_{\mathrm{DW,x}} \mathbf{u}_{\mathrm{z}},$$

which points along the easy axis (u_z) with a magnitude proportional to the x-component of the internal DW magnetization $\mathbf{m}_{DW,x}$ (where $\mathbf{m}_{\mathrm{DW}} = \mathrm{m}_{\mathrm{DW,x}}\mathbf{u}_{\mathrm{x}} + \mathrm{m}_{\mathrm{DW,y}}\mathbf{u}_{\mathrm{y}}$ is the internal DW magnetization in general). Fig. 3(d) indicates that for a given value of the applied current j_a, the ↑↓-DW remains pinned between an asymmetric longitudinal field range [$H_{d,-}$,$H_{d,+}$] with |$H_{d,-}$| > |$H_{d,+}$|: from $\mu_\circ H_{d,-}$=-15 mT to $\mu_\circ H_{d,+}$=-5 mT for j_a=3.6x10^{11} A/m^2; and from $\mu_\circ H_{d,-}$=-15 mT to $\mu_\circ H_{d,+}$=0 mT for j_a=2.8x10^{11} A/m^2. As a positive longitudinal field (H_x>0) is parallel to the internal DW magnetization of an ↑↓-DW at rest ($m_{DW,x}$>0), such a field stabilizes the Néel configuration of the DW against the initial rotation of $\mathbf{m}_{DW}$ due to the current-induced torque, increasing the effective SHE field (H_{SHE}) and therefore supporting DW depinning. This results in a DW motion against the electron flow as in the absence of longitudinal field (e.g., with positive velocity for j_a>0). On the contrary, a negative longitudinal field (H_x<0) is anti-parallel to the internal DW magnetization of the right-handed ↑↓-DW at rest ($m_{DW,x}$>0), and consequently it reduces the magnitude of $m_{DW,x}$ and H_{SHE}. Therefore, H_x<0 acts against DW depinning which explains the experimental observation that for a given current |$H_{d,-}$| > |$H_{d,+}$|. The depinning field $\mu_\circ H_{d,-}$ is larger than the DMI effective field (|$\mu_\circ H_{d,-}$| >

$\mu_o H_{DMI}=D/(M_S\Delta)$), so that when such a field is reached the direction of the DW motion reverses, being now along the electron flow. This explanation is also valid for the ↓↑-DW, where the internal DW magnetization is $m_{DW,x}<0$ at rest. In this case, the critical depinning values satisfy $|H_{d,+}| > |H_{d,-}|$ because it is now a negative longitudinal field ($H_x<0$) parallel to $m_{DW,x}$ which supports the DW depinning and subsequent propagation along the conventional current flow (see Fig. 3(c)).

VII. CONCLUSIONS

Current-induced domain wall motion is observed in Ta\$Co_{20}Fe_{60}B_{20}$\MgO nanowires, where the domain walls move against the electron flow. The DW velocity is strongly influenced by a magnetic field applied along the wires. Moving from negative to positive applied magnetic fields the DW velocity changes its magnitude and in its direction, in agreement with the SOT-model. A DMI-effective field $\mu_o H_{DMI}=+7.8\pm1.2$ mT is observed, resulting in a DMI constant $D=+0.06\pm0.01$ mJ/m^2, corresponding to right-handed DWs in our materials system. The positive DMI coefficient is attributed to the diffusion of B in the Ta buffer layer and its segregation at the Ta\$Co_{20}Fe_{60}B_{20}$ interface which we directly observed by chemical depth profiling. This is in line with recent explanations using the electronegativity of the elements at the interface as a key parameter. Using 1D-model simulations we are able to reproduce the experimental data if we include pinning effects and we extract a spin-Hall angle of $\theta_{SH}=-0.11$ for Ta.

ACKNOWLEDGMENTS

We acknowledge support by the Graduate School of Excellence Materials Science in Mainz (MAINZ) GSC 266, Staudinger Weg 9, 55128, Germany; the EU (IFOX, NMP3-LA-2012 246102; MASPIC, ERC-2007-StG 208162; WALL, FP7-PEOPLE-2013-ITN 608031; MAGWIRE, FP7-ICT-2009-5), and the Research Center of Innovative and Emerging Materials at Johannes Gutenberg University (CINEMA). This work was also supported by EPSRC, U.K. (Grant Nos. EP/I011668/1, EP/K003127/1, EP/L00285X/1) and the Alexander von Humboldt Foundation CONNECT program.

E. M. acknowledge the support by project MAT2011-28532-C03-01 from Spanish government and project SA163A12 from Junta de Castilla y Leon. Finally, we also thank the Singulus Technologies AG for support with the materials stacks preparation.

FIGURE CAPTIONS

FIG. 1. (a) Schematic of the experimental set-up for current pulse injection, including an SEM micrograph of the sample used during the experiment. The inset shows the shape of one of the pulses applied to the device, measured with the oscilloscope (across the 50 Ω internal resistance). (b) Differential Kerr microscopy image of nucleated magnetic domains by Oersted-field in initialized nanowires. The magnetization in the reversed domains is pointing upwards (+z, black areas). (c) Differential Kerr microscopy image of the same wires in (b), after domain walls motion by injecting a burst of 50 current pulses (Δt=25 ns, j_a=-2.75x10^{11} A/m^2, j_a>0 in the +x direction) through the nanowires. The direction of the applied conventional current j_a and of the electron current j_e is indicated by the red and blue arrow respectively.

FIG. 2. (a) Average velocity of the DW as a function of the current density injected in the magnetic wires, for different durations of the current pulse. The DW velocity increases with the pulse duration, due to the fact that the 5 ns rise- and fall-time of the injected pulses have less influence on the measured domain wall velocity during longer pulses. The DW moves with the conventional current j_a (against the electron flow j_e). The average velocities and the error bars (standard deviations) are calculated from 30 different DW motions, at each current density. (b) Average velocity of the DW as a function of j_a, free of the rise- and fall-time influence.

FIG. 3. Effect of a longitudinal magnetic field on the current-induced DW motion. (a) Differential Kerr microscopy image of nucleated magnetic domains in pre-saturated nanowires. The magnetization in the reversed domains points in the +z direction (black areas). The green lines indicate the position of the DWs. The red arrows describe the DWs magnetization configuration. (b) Differential Kerr microscopy image of the domain walls moved due to current pulse injection (j_a=+3.6x10^{11} A/m^2), when a longitudinal field is applied ($\mu_\circ H_x$=-35 mT). The dashed green lines indicate the starting position of the DWs, while the solid orange lines indicate their final position. The blue arrows show the DW motion. Down-up (DU, ↓↑) and up-down (UD, ↑↓) DWs move in opposite direction. (c) Average velocity of ↓↑- and (d) ↑↓-DWs as a function of the longitudinal field ($\mu_\circ H_x$), for two different current densities. Solid symbols refer to j_a=3.6x10^{11} A/m^2, while empty

symbols refer to j_a=2.8x10^{11} A/m^2. Squares refer to positive j_a, while triangles refer to negative j_a. The solid (dashed) lines are the 1D-model fitting-curves for j_a=±3.6x10^{11} A/m^2 (j_a=±2.8x10^{11} A/m^2) (see text for details). (e) Average velocity of ↓↑- (empty symbols) and ↑↓- (solid symbols) domain walls as a function of $\mu_o H_x$, for a current density of j_a=+3.6x10^{11} A/m^2 (squares), and j_a=-3.6x10^{11} A/m^2 (triangles). Lines represent the 1D-model fitting-curves.

FIG. 4. (a) TEM cross-section image of the Ta(5)\$Co_{20}Fe_{60}B_{20}$(1)\MgO(2)\Ta(5) stack showing that MgO and CoFeB crystallize in the cubic phase after annealing. Marks indicating the different layers are superimposed as a guide to the eye. Layer thicknesses are reported in nm. (b) SIMS depth profiles of as-deposited (ad) and annealed (ann) (300°C, 2h) structures. Signals related to B (dots), MgO (squares), Fe (up-triangles) and Co (down-triangles) are shown. Following the B profile, the presence of B diffusion from $Co_{20}Fe_{60}B_{20}$ layer towards the Ta layer (and partially the MgO layer) is evidenced. For the sake of clarity profiles are aligned at $Co_{20}Fe_{60}B_{20}$\Ta interface. Secondary ions are collected in negative mode, and the measurement parameters are as reported in [38].

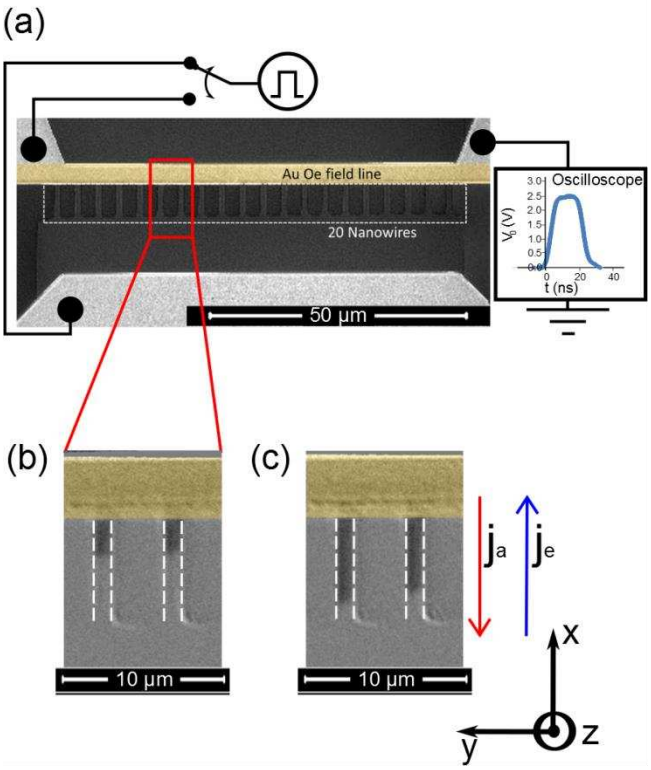
(a)
Au Oe field line
20 Nanowires
50 µm
Oscilloscope
V_0 (V)
t (ns)
(b)
10 µm
(c)
10 µm
j_a
j_e
x
y
z

Figure 1

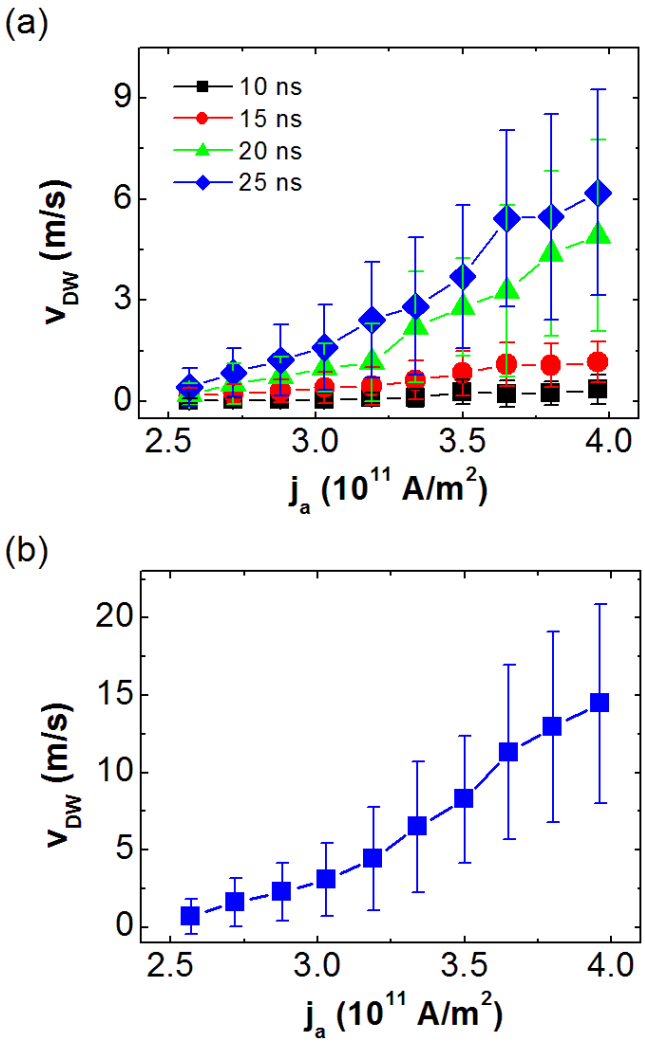

Figure 2

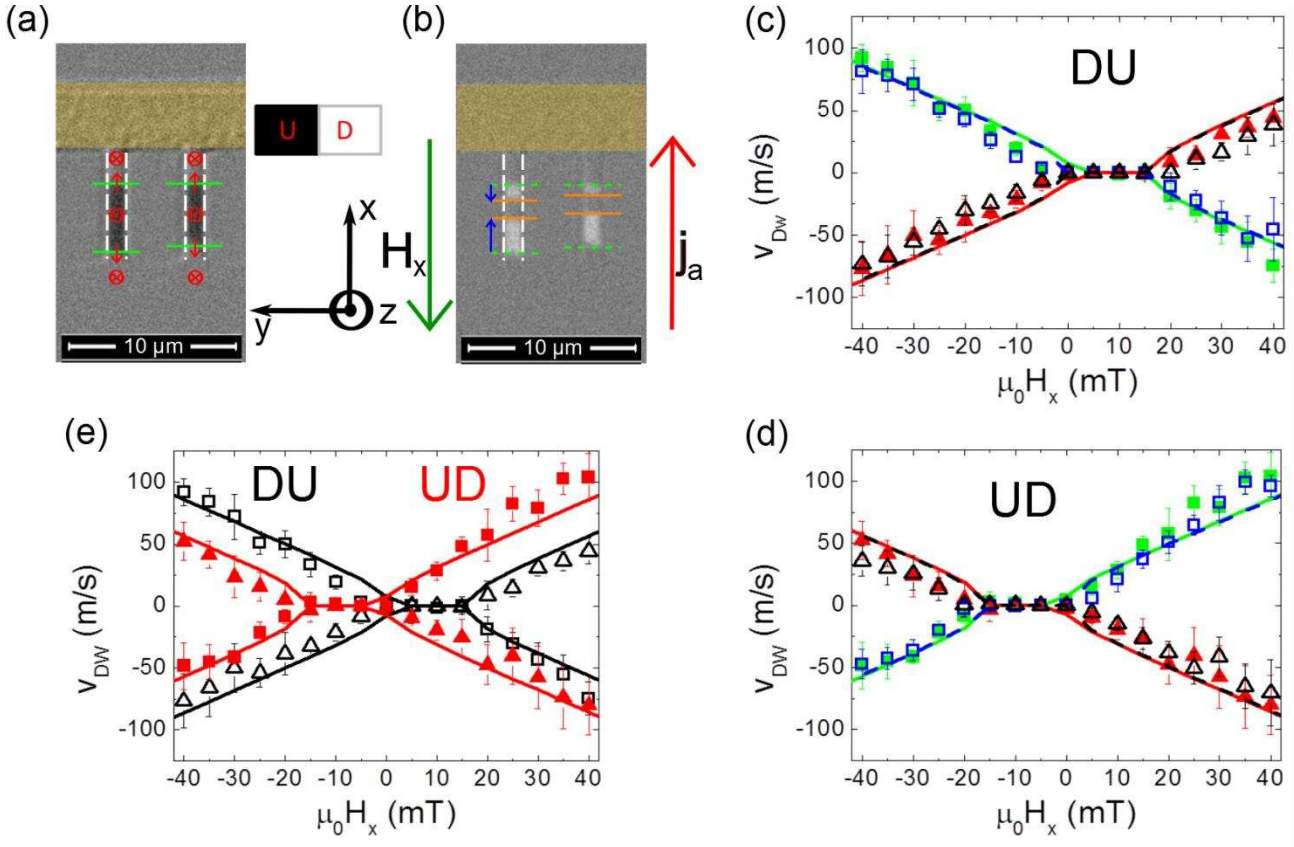
(a)
(b)
(c)
U
D
x
H_x
z
y
j_a
10 µm
10 µm
DU
v_Dw (m/s)
µ_0H_x (mT)
(e)
DU
UD
v_DW (m/s)
µ_0H_x (mT)
(d)
UD
v_DW (m/s)
µ_0H_x (mT)

Figure 3

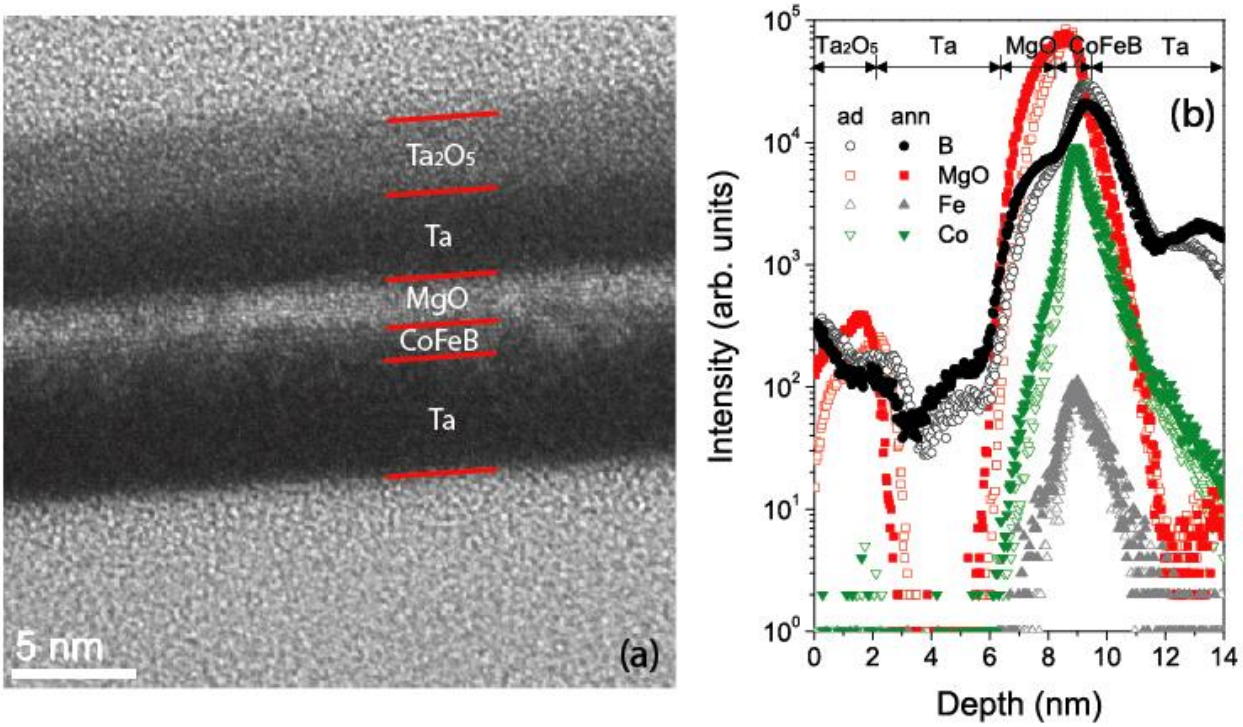
Ta2O5
Ta
MgO
CoFeB
Ta
5 nm
(a)
Ta2O5
Ta
MgO
CoFeB
Ta
(b)
ad
ann
B
MgO
Fe
Co
Intensity (arb. units)
Depth (nm)

Figure 4

References

[1] J. M. D. Coey, *Magnetism and Magnetic Materials*, Cambridge University Press (2009).

[2] S. S. P. Parkin, M. Hayashi, and L. Thomas, *Magnetic Domain-Wall Racetrack Memory*, Science **320**, 190-194 (2008).

[3] K.-S. Ryu, L. Thomas, S.-H. Yang, and S.S.P. Parkin, *Chiral spin torque at magnetic domain walls*, Nature Nanotech. **8**, 527-533 (2013).

[4] O. Boulle, G. Malinowski, and M. Kläui, *Current-induced domain wall motion in nanoscale ferromagnetic elements*, Mat. Sci. Engin. **R 72**, 159-187 (2011).

[5] T. A. Moore, I. M. Miron, G. Gaudin, G. Serret, S. Auffret, B. Rodmacq, A. Schuhl, S. Pizzini, J. Vogel, and M. Bonfim, *High domain wall velocities induced by current in ultrathin Pt/Co/AlOx wires with perpendicular magnetic anisotropy*, Appl. Phys. Lett. **93**, 262504 (2008).

[6] I. M. Miron, G. Gaudin, S. Auffret, B. Rodmacq, A. Schuhl, S. Pizzini, J. Vogel, and P. Gambardella, *Current-driven spin torque induced by the Rashba effect in a ferromagnetic metal layer*, Nature Mater. **9**, 230-234 (2010).

[7] I. M. Miron, T. Moore, H. Szambolics, L. D. Buda-Prejbeanu, S. Auffret, B. Rodmacq, S. Pizzini, J. Vogel, M. Bonfim, A. Schuhl and G. Gaudin, *Fast current-induced domain-wall motion controlled by the Rashba effect*, Nature Mater. **10**, 419-423 (2011).

[8] K. Garello, I.M. Miron, C.O. Avci, F. Freimuth, Y. Mokrousov, S. Blügel, S. Auffret, O. Boulle, G. Gaudin, and Pietro Gambardella, *Symmetry and magnitude of spin-orbit torques in ferromagnetic heterostructures*, Nature Nanotech. **8**, 587-593 (2013).

[9] S. Emori, U. Bauer, S.-M. Ahn, E. Martinez, and G. S. D. Beach, *Current-driven dynamics of chiral ferromagnetic domain walls*, Nature Mater. **12**, 611-616 (2013).

[10] S. Fukami, T. Suzuki, Y. Nakatani, N. Ishiwata, M. Yamanouchi, S. Ikeda, N. Kasai, and H. Ohno, *Current-induced domain wall motion in perpendicularly magnetized CoFeB nanowire*, Appl. Phys. Lett. **98**, 082504 (2011).

[11] J. Kim, J. Sinha, M. Hayashi, M. Yamanouchi, S. Fukami, T. Suzuki, S.Mitani, and H. Ohno, *Layer thickness dependence of the current-induced effective field vector in Ta|CoFeB|MgO*, Nature Mater. **12**, 240-245 (2012).

[12] C.O. Avci, K. Garello, C. Nistor, S. Godey, B. Ballesteros, A. Mugarza, A. Barla, M. Valvidares, E. Pellegrin, I.M. Miron, O. Boulle, S. Aufrett, G. Gaudin, and P. Gambardella, *Field-like and anti-damping spin-orbit torques in as-grown and annealed Ta/CoFeB/MgO layers*, Phys. Rev. B **89**, 214419 (2014).

[13] X. Qiu, P. Deorani, K. Narayanapillai, K.-S. Lee, K.-J. Lee, H.-W. Lee, and H. Yang, *Angular and temperature dependence of current induced spin-orbit effective fields in Ta/CoFeB/MgO nanowires*, Scientific Reports **4**, 4491 (2014).

[14] L. Liu, O.J. Lee, T.J. Gudmundsen, D.C. Ralph, and R.A. Buhrman, *Current-Induced Switching of Perpendicularly Magnetized Magnetic Layers Using Spin Torque from the Spin Hall Effect*, Phys. Rev. Lett. **109**, 096602 (2012).

[15] I. M. Miron, K. Garello, G. Gaudin, P.-J. Zermatten, M.V. Costache, S. Auffret, S. Bandirra, B. Rodmacq, A. Schuhl, and P. Gambardella, *Perpendicular switching of a single ferromagnetic layer induced by in-plane current injection*, Nature **476**, 189-193 (2011).

[16] C.O. Avci, K. Garello, I.M. Miron, G. Gaudin, S. Aufrett, O. Boulle, and P. Gambardella, *Magnetization switching of an MgO/Co/Pt layer by in-plane current injection*, Appl. Phys. Lett. **100**, 212404 (2012).

[17] R. Lo Conte, A. Hrabec, A.P. Mihai, T. Schulz, S.-J. Noh, C.H. Marrows, T.A. Moore, and M. Kläui, *Spin-orbit torque-driven magnetization switching and thermal effects studied in Ta\CoFeB\MgO nanowires*, Appl. Phys. Lett. **105**, 122404 (2014).

[18] Y. A. Bychkov, and E. I. Rashba, *Oscillatory effects and the magnetic susceptibility of carriers in inversion layers*, J. Phys. C.: Solid State Phys. **17**, 6039-6045 (1984).

[19] M. I. Dyakonov, and V. I. Perel, *Possibility of orienting electron spins with current*, ZhETF Pis. Red. 13, No. 11, 657-660 (1971).

[20] M. I. Dyakonov, and V. I. Perel, *Current-induced spin orientation of electrons in semiconductors*, Phys. Lett. **35A**, n. 6 (1971).

[21] A. Fert, *Magnetic and transport properties of metallic multilayers*, Mat. Sci. Forum **50-60**, 439-480 (1990).

[22] A. Thiaville, S. Rohart, E. Jué, V. Cros, and A. Fert, *Dynamics of Dzyaloshinskii domain walls in ultrathin magnetic films*, Europhys. Lett. **100**, 57002 (2012).

[23] S.Ikeda, J.Hayakawa, Y. M. Lee, F. Matsukura, Y. Ohno, T. Hanyu, and H. Ohno, *Magnetic Tunnel Junctions for Spintronic Memories and Beyond*, IEEE Trans. Electron Devices **54**(5), 991-1002 (2007).

[24] O. Boulle, G. Malinowski, and M. Kläui, *Current-induced domain wall motion in nanoscale ferromagnetic elements*, Mater. Sci. Eng. R **72**, 159-187 (2011).

[25] J. Torrejon, J. Kim, J. Sinha, S. Mitani, M. Hayashi, M. Yamanouchi, and H. Ohno, *Interface control of the magnetic chirality in CoFeB/MgO heterostructures with heavy-metal underlayers*, Nature Comm. **5**, 4655 (2014).

[26] A. Hrabec, N. A. Porter, A. Wells, M. J. Benitez, G. Burnell, S. McVitie, D. McGrouther, T. A. Moore, and C. H. Marrows, *Measuring and tailoring the Dzyaloshinskii-Moriya interaction in perpendicularly magnetized thin films*, Phys. Rev. B **90**, 020402 (R) (2014).

[27] L. Liu, C.-F. Pai, Y. Li, H.-W. Tseng, D.C. Ralph, and R.A. Buhrman, *Spin-Torque Switching with the Giant Spin Hall Effect of Tantalum*, Science **336**, 555 (2012).

[28] S. Emori, E. Martinez, U. Bauer, S. M. Ahn, P. Agrawal, D. C. Bono, and G. S. D. Beach, *Spin Hall torque magnetometry of Dzyaloshinskii domain walls*, arXiv:1308.1432 **[cond-mat.mtrl-scil]** (2013).

[29] A. Lamperti, S.-M. Ahn, B. Ocker, R. Mantovan, and D. Ravelosona, *Interface width evaluation in thin layered CoFeB/MgO multilayers including Ru or Ta buffer layer by X-ray reflectivity*, Thin Solid Films **533**, 79–82 (2013).

[30] H. Bouchikhaoui, P. Stender, D. Akemeier, D. Baither, K. Hono, A. Hütten, and G. Schmitz, *On the role of Ta cap in the recrystallization process of CoFeB layers*, App. Phys. Lett. **103**, 142412 (2013).

[31] G. Yu, P. Upadhyaya, K. L. Wong, W. Jiang, J. G. Alzate, J. Tang, P. K. Amiri, and K. L. Wang, *Magnetization switching through spin-Hall-effect-induced chiral domain wall propagation*, Phys. Rev. B 89, 104421 (2014).

[32] See Supplemental Material at [*URL will be inserted by publisher*] for CIDWM in Pt\CoFeB\MgO sample.

[33] E. Martinez, S. Emori, N. Perez, L. Torres, and G.S.D. Beach, *Current-driven dynamics of Dzyaloshinskii domain walls in the presence of in-plane fields: Full micromagnetic and one-dimensional analysis*, J. Appl. Phys. **115**, 213909 (2014).

[34] S.V. Tarasenko, A. Stankiewicz, V.V. Tarasenko, and J. Ferre, *Bloch wall dynamics in ultrathin ferromagnetic films*, J. Magn. Magn. Mater. **189**, 19 (1998).

[35] S. Iihama, S. Mizukami, H. Naganuma, M. Oogane, Y. Ando, and T. Miyazaki, *Gilbert damping constants of Ta/CoFeB/MgO(Ta) thin films measured by optical detection of precessional magnetization dynamics*, Phys. Rev. B **89**, 174416 (2014).

[36] L. Liu, T. Moriyama, D. C. Ralph, and R. A. Buhrman, *Spin-Torque Ferromagnetic Resonance Induced by the Spin Hall Effect*, Phys. Rev. Lett. **106**, 036601 (2011).

[37] E. Martinez, *The stochastic nature of the domain wall motion along high perpendicular anisotropy strips with surface roughness*, J. Phys.: Condens. Matter. **24**, 024206 (2012).

[38] A. Lamperti, E. Cianci, O. Salicio, L. Lamagna, S. Spiga, and M. Fanciulli, *Thermal stability of high-k oxides on SiO2/Si or SixNy/SiO2/Si for charge-trapping nonvolatile memories*, Surf. Interf. Analys. **45**, 390–393 (2013).